| Title | Origin of the surface facet dependence in the thermal degradation of the diamond (111) and (100) surfaces in vacuum investigated by machine learning molecular dynamics simulations |
|---|---|
| Author(s) | Enriquez, John Isaac G.; Halim, Harry Handoko; Yamasaki, Takahiro et al. |
| Citation | Carbon. 2024, 226, p. 119223 |
| Version Type | VoR |
| URL | https://hdl.handle.net/11094/97167 |
| rights | This article is licensed under a Creative Commons Attribution 4.0 International License. |
| Note | |

# Origin of the surface facet dependence in the thermal degradation of the diamond (111) and (100) surfaces in vacuum investigated by machine learning molecular dynamics simulations

John Isaac G. Enriquez [a], Harry Handoko Halim [a], Takahiro Yamasaki [b], Masato Michiuchi [b], Kouji Inagaki [a], Masaaki Geshi [c], Ikutaro Hamada [a], Yoshitada Morikawa [a,d,*]

[a] Department of Precision Engineering, Graduate School of Engineering, Osaka University, 2-1 Yamadaoka, Suita, Osaka, 565-0871, Japan
[b] Advanced Materials Laboratory, Sumitomo Electric Industries, Ltd, Itami, Hyogo, 664-0016, Japan
[c] R³ Institute for Newly-Emerging Science Design, Osaka University, 1-2 Machikaneyama, Toyonaka, Osaka, 560-0043, Japan
[d] Research Center for Precision Engineering, Graduate School of Engineering, Osaka University, 2-1 Yamada Oka, Suita, Osaka, 565-0871, Japan

## ABSTRACTSS

We perform machine learning molecular dynamics simulations to gain an atomic-level understanding of the dependence of the graphitization and thermal degradation behavior of diamond to the (111) and (100) surface facets. The interatomic potential is constructed using graph neural network model, trained using energies and forces from spin-polarized van der Waals-corrected density functional theory calculations. Our results show that the C(111) surface is more susceptible to thermal degradation, which occurs from 2850 K through synchronized bilayer exfoliation mechanism. In comparison, the C(100) surface thermally degrade from a higher temperature of 3680 K through the formation of $sp^1$ carbon chains and amorphous $sp^2$-$sp^3$ carbon network. Due to the dangling bonds at the step edges, the stepped surfaces are more susceptible to thermal degradation compared to the corresponding flat surfaces, with the stepped C(111) and C(100) surfaces thermally degrading from 1810 K to 3070 K, respectively. We propose potential applications of this study in diamond tool wear suppression, diamond polishing, and production of graphene directly from the diamond surface.

## 1. Introduction

Diamond is an ideal material for a variety of high-technology applications due to its exceptional characteristics, such as its extreme hardness, chemical inertness, high dielectric breakdown strength and carrier mobility, optical transparency, and quantum coherence [1–5]. Diamond is a thermodynamically unstable form of carbon, and when heated to sufficiently high temperatures, changes into graphite [6]. This thermal degradation process, which is commonly referred to as graphitization, typically produces not just crystalline graphite but also amorphous carbon [7,8]. The transformation of diamond to graphite and other amorphous $sp^2$-$sp^3$ materials occurs in several industrial and device fabrication processes such as diamond tool wear [9], catalytic etching [10], polishing [11], laser ablation [12], and plasma treatment [13]. The most technologically important diamond facets are the (111) and (100) surfaces [14]. An experiment on synthetic diamond microcrystals have shown that the diamond (111) surface [C(111)] is more

susceptible to graphitization compared to the (100) surface [15]. The atomistic mechanism of the dependence of the thermal degradation on the diamond surface facets has yet to be elucidated. Understanding this mechanism will enable surface-specific processing and design of diamond devices and benefit several engineering applications in which graphitization is desired to either be precisely controlled or totally prevented.

Atomistic simulations of the graphitization of the C(111) surface have been performed in the past using ab-initio molecular dynamics (AIMD) [16]. Even though AIMD is one of the most accurate materials simulation method, it is only possible to simulate small systems for a very short simulation time because of high computational cost. For instance, the C(111) surface models in the study have only around 100 atoms, with simulation time of less than 10 ps and heating rate in the order of 1000 K/ps. The limitation in the simulation size and time scale could have caused the overestimated graphitization temperature of the flat (3500–3900 K) and stepped C(111) surfaces (2500 K), which are

much higher compared to the experiment value, where the graphitization occurs between 1600 and 1700 °C (1873–1973 K) depending on the heating rate and time [6,15,17,18]. Furthermore, the thermal degradation of the diamond (100) surface [C100] has never been simulated using AIMD to the best of our knowledge.

A larger and more realistic system model and longer simulation time is necessary to perform simulations that will demonstrate the surface facet dependence of the thermal degradation. However, this will be very computationally demanding to do using AIMD. A possible alternative is to use classical molecular dynamics (MD) simulations using e.g., Tersoff, REBO, ReaxFF, and EDIP potentials. However, a comparative study has shown that these potentials do not agree well with one another on the predicted results for both annealed and amorphous carbon. Thus, the reliability and transferability of any of these classical potentials are difficult to assess [19]. This will be especially true in simulations involving diamond-to-graphite phase transformation. In addition, existing classical MD studies on diamond graphitization [20,21] were not able to demonstrate the formation of $sp^1$-hybridized carbon chains and amorphous carbon that were observed in experiments [7,22,23].

Recently, machine learning interatomic potentials (ML-IPs) trained on forces and energies calculated from ab-initio methods such as density functional theory (DFT) have been developed and used to perform machine learning molecular dynamics (MLMD) simulations. The MLMD method has two main advantages over classical MD. First, the MLMD method allows large-scale and long time-scale simulations with higher accuracies, practically comparable to the AIMD method. Second, the non-equilibrium and amorphous structures obtained from the simulations can be used as training data to fine tune the ML-IP in the process called active learning, ensuring the reliability of the potential even if bond breaking and phase change occurs during the simulation. Among various MLMD methods, the equivariant graph neural networks (GNN) implemented in the NequIP software uses graph message passing analogous to the convolution filters used in image recognition neural network models [24]. Unlike the earlier neural network methods that uses fixed 2- and 3-body symmetry functions [25], the GNN method captures many body interactions. This makes GNN interatomic potentials (GNN-IPs) considerably more accurate compared to other ML-IPs of several molecules and materials. The GNN-IPs trained using NequIP software have been used to study several materials and chemical systems, including liquid water and ice dynamics [24], formate dehydrogenation [24], kinetic transport simulations [24], adsorption of $CO_2$ on metal organic frameworks [26], reactivity of single atom alloy nanoparticles [27], lattice thermal conductivity calculations [28], and aqueous electrolyte structure prediction [29].

In this work, we perform MLMD simulations of the C(111) and C(100) surfaces in vacuum using GNN-IPs. Our objectives are (1) to investigate how carbon chains and amorphous carbon form on diamond surfaces at high temperatures and (2) to elucidate the difference in the thermal degradation susceptibility of the flat and stepped diamond (111) and (100) surfaces.

## 2. Computational methodology

### 2.1. Graph neural network interatomic potential construction

We started the construction of GNN-IP by building an initial database of equilibrium structures consisting of diamond, graphite, graphene, and flat and stepped diamond (111) and (100) surfaces (Supplementary Document Fig. S1). From the equilibrium structures, non-equilibrium structures are generated by randomizing the atomic coordinates, annealing at various temperatures using AIMD and MLMD, and performing active learning as described in Section 2.2. The non-equilibrium structures generated through the active learning include thermally degraded C(111) surfaces with exfoliated top bilayer and C(100) surfaces with amorphous carbon and carbon-chain on the surface. The forces and energies of these structures are calculated using DFT and used

for training the GNN-IP model. Each structure sample $i$ on the database consist of the atomic positions $r_{ix}$, $r_{iy}$, and $r_{iz}$, force components $F_{ix}$, $F_{iy}$, and $F_{iz}$, and total potential energy $E_i$ of the simulation system. The database of structures used in the construction of GNN-IP are provided in the Supplementary Material.

The NequIP software is used to construct a GNN-IP that maps the atomic positions and chemical species to the potential energy of the simulation system and forces acting on the atoms [24]. In this method, the nodes in the graph represents the individual atoms while the edges are defined by connecting every atom to all other atoms within a cutoff radius. Every atom is described by a feature vector which is refined by message passing through convolution layers. Rotational equivariance is achieved by constraining the convolution to be products of radial function and spherical harmonics with learnable weights. The radial function is constructed as the product of Bessel function and polynomial cutoff function. We use a total of 8 radial basis and polynomial order of 6. The network has 32 features with 4 interaction blocks and a max tensor rank of 1. The cutoff radius is set to 4.0 Å which is larger than the 5th nearest neighbor in bulk diamond and the distance between adjacent graphite layers. The cutoff radius is large enough to accurately describe the activation energy of bilayer exfoliation on the C(111) surface (Section 3.2). The predicted total potential energy is obtained by the sum of atomic contributions and the energy conservation is guaranteed by calculating the predicted force from the gradient of predicted energy. The GNN interatomic potential is trained using the loss function based on the weighed sum of the energy and force loss terms where we set both weights to 1.0. The database is split such that 90 % of the data is used to training the weights and biases and the remaining 10 % is used for testing.

### 2.2. Graph neural network interatomic potential fine-tuning and evaluation

The constructed GNN-IP is evaluated based on its (1) accuracy, (2) stability, and (3) reliability.

1. The accuracy of the GNN-IP is based on the root mean square error (RMSE) of the forces and energies of the test data. Accuracies can be improved by adjusting the training hyperparameters such as the learning rate and size of the network.
2. The stability of the GNN-IP refers to the ability to simulate at the target temperature for sufficiently long timescales without misbehaving or crashing. A misbehaved simulation includes explosions of systems, temperature spikes, and formation of unphysical structures. We observe that crashes of simulations typically occur right after the formation of atomic environments that are not well represented in the database. The stability of the GNN-IP is improved by adding these new atomic environments and structures to the database.
3. Machine learning of interatomic potential is a kind of regression modelling. As with all regression methods, the predictions are more reliable in interpolating between datapoints and less reliable in extrapolating. An extrapolated atomic environment means that the atomic environment is not correlated with any atomic environment on the database. In other words, the database does not contain training data for such configuration of atoms. We use this principle in checking for extrapolated atomic environment. First, we make a database of the feature vectors of all the atomic environment in our dataset. The feature vectors were calculated using neural message passing [30]:

$$\mathbf{h}_i^{(0)} = \mathbf{x}_i \tag{1}$$

$$\mathbf{h}_i^{(k+1)} = \text{UPDATE}^{(k)} \left( \text{AGGREGATE}^{(k)} \left( \left\{ \mathbf{h}_j^{(k)}, \forall j \in \mathcal{N}(i) \right\} \right) \right) \tag{2}$$

where $\mathbf{x}_i$ is the initial embedding chosen depending on the atomic species, $\mathbf{h}_i$ is the hidden embedding of atom $i$, and $k$ is the number of message passes. The aggregate function is a function of the hidden embeddings of the neighboring atoms $j$, and takes the form

$$\text{AGGREGATE}\left(\mathbf{h}_j^{(k)}\right) = \tanh\left(S_m^l\right) \tag{3}$$

$$S_m^l = \sum_{i \neq j}^{N} R\left(r_{ij}\right) f\left(r_{ij}, r_c\right) Y_m^l\left(\widehat{r}_{ij}\right) \tag{4}$$

$$R\left(r_{ij}\right) = \frac{2}{r_c} \frac{\sin\left(\frac{b\pi}{r_c} r_{ij}\right)}{r_{ij}} \tag{5}$$

$$f\left(r_{ij}, r_c\right) = 1 - \frac{(p-1)(p+2)}{2}\left(\frac{r_{ij}}{r_c}\right)^p + p(p+2)\left(\frac{r_{ij}}{r_c}\right)^{p+1} - \frac{p(p+1)}{2}\left(\frac{r_{ij}}{r_c}\right)^{p+2} \tag{6}$$

Here, $R\left(r_{ij}\right)$, $f\left(r_{ij}, r_c\right)$, and $Y_m^l\left(\widehat{r}_{ij}\right)$ are the Bessel radial basis function, polynomial cutoff function, and spherical harmonics, respectively. The feature vectors are updated using the equation

$$\text{UPDATE}^{(k)}\left(\text{AGGREGATE}\left(\mathbf{h}_j^{(k)}\right)\right) = \mathbf{h}_i^{(k)} + \text{AGGREGATE}\left(\mathbf{h}_j^{(k)}\right) \tag{7}$$

Second, we use the GNN-IP to perform MD simulations. Then we calculated the feature vectors of the atomic environments on an MD snapshot. We compare each feature vector element to the database. If we found elements whose numerical value is lower or higher than the maximum value of the corresponding feature vector in the database, then we regard the atomic environment as extrapolated. The forces and energies of the structures containing the extrapolated atomic environments are calculated using DFT added to the database.

After the new structures have been added into the database, a new GNN-IP is trained and used to perform MD simulations. The accuracy, stability, and reliability are evaluated using the criteria described above. We continue this cycle to improve the interatomic potential iteratively or through an active learning process, until all of the GNN-IP evaluation criterion is satisfied.

### 2.3. Graph neural network interatomic potential pre-production validation

A novel feature of our simulation is the implementation of pre-production validation. In pre-production validation, we simulated a smaller system with the same conditions such as heating rate and temperature range that we plan on doing on the production simulations. The smaller system size allowed us to calculate DFT forces and energies of sampled MD snapshots and perform a final error analysis and validation. We performed the GNN-IP pre-production validation by simulating the C(111) and C(100) surfaces at increasing temperatures, up to 3600 K for the C(111) and 4400 K for the C(100). The chosen maximum temperatures are higher than the predicted thermal degradation temperatures through test calculation using earlier versions of the GNN-IP models. Simulations using the final version of the GNN-IP model confirm that the thermal degradation temperatures of the C(111) and C(100) are within the temperature range considered in the pre-production validation. The pre-production simulation models are shown in Table 1. Then, we selected 260 MD snapshots and calculate the DFT forces and energies which we then compared with the ones predicted by the GNN-IP. Finally, we evaluated the reliability by checking if there are any extrapolated atomic environments.

**Table 1**

Diamond surface models for pre-production validation and production simulations, showing the simulation box sizes x and y and the number of atoms in each structure.

| Type of Surface | x (Å) | y (Å) | No. of Atoms |
|---|---|---|---|
| Pre-Production Validation | | | |
| Flat C(111) (4 × 4) | 8.7488 | 10.1023 | 208 |
| Flat C(100) (4 × 4) | 10.1023 | 10.1023 | 208 |
| Production Simulation | | | |
| Flat C(111) (8 × 8) | 17.4977 | 20.2046 | 832 |
| Stepped C(111)/C(665) | 24.8761 | 20.2046 | 1184 |
| Flat C(100) (8 × 8) | 20.2046 | 20.2046 | 832 |
| Stepped C(100)/C(1 1 10) Type A | 25.5071 | 20.2046 | 1000 |
| Stepped C(100)/C(1 1 10) Type B | 25.5071 | 20.2046 | 1048 |

### 2.4. Density functional theory calculations and molecular dynamics simulations

The forces and energies are calculated using spin-polarized DFT calculations [31] using STATE code package (Simulation Tool for Atom TEchnology) [32,33] with the generalized gradient exchange correlation functional based on the work of Perdew, Burke, and Ernzerhof (GGA-PBE) [34] and the Grimme D2 dispersion correction [35]. We use ultra-soft pseudopotential to treat core electrons [36]. We expand the wave functions and augmentation charge using plane wave basis with cutoffs of 36 Ry (490 eV) and 400 Ry (5442 eV), respectively. Special points for Brillouin-zone integration were generated using the Monkhorst-Pack scheme [37]. The convergence threshold for energy minimization is $1.0 \times 10^{-9}$ Ha/atom ($2.72 \times 10^{-8}$ eV/atom). We perform geometry optimizations until the forces on each atom is less than $1.0 \times 10^{-3}$ Ha/$a_0$ ($5.14 \times 10^{-2}$ eV/Å). The number of k-point depends on the simulation cell size and were all tested for convergence. All calculations were performed using Born-Oppenheimer approximation with zero electronic temperature. Zero-electronic temperature approximation has been used to study carbon phase diagrams at extreme pressures and temperatures and comparison with finite-electronic temperature shows minimal error especially for insulating systems [38]. Similar approximation was done on a recent MLMD study of carbon at extreme pressures and temperatures, which shows highly accurate prediction of Hugoniot temperatures (temperature attained of a material during shockwave compression) particularly for temperatures <10,000 K [39].

Molecular dynamics simulations are performed on LAMMPS code [40] using an NVT ensemble with Nose-Hoover thermostat and a timestep of 0.1 fs [41]. In this method, the temperature of the atomic nuclei is controlled by first calculating the nuclei velocities using the GNN-IP and then introducing a fictitious dynamical variable which slows or accelerates the particles until desired temperature, calculated using the equipartition function, is reached. Periodic boundary conditions are imposed along the x and y axis. The simulation models of the flat and stepped diamond (111) and (100) surfaces for production calculations are shown in Table 1 and Fig. 1. The C(100) surface reconstruction by C-atom dimerization is not a thermally activated process and occurs spontaneously at 0 K [42]. For this reason, all simulations of the C(100) surface start with the reconstructed model. We consider two types of stepped C(100), depending on whether the dimer direction is normal (Type A) or parallel (Type B) to the step edge. The main difference between these two stepped surface models is the absence (Type A) or presence (Type B) of dangling bonds on the second layer of the step edge, similar to the stepped Si(001) models proposed by Chadi [43]. Our test calculations show that a slab model thickness of 12 layers is sufficient to describe the surface reconstruction, bilayer exfoliation and reconstruction, which is the energy difference between a C(111) surface and C(111) surface with graphitized top 2 layers, and the surface energies. Increasing the thickness to 16 layers have negligible effect on these properties (Table 2). All models have 12C layers, and the bottom atoms are terminated with H atoms. The bottom 2 layers and the H layer
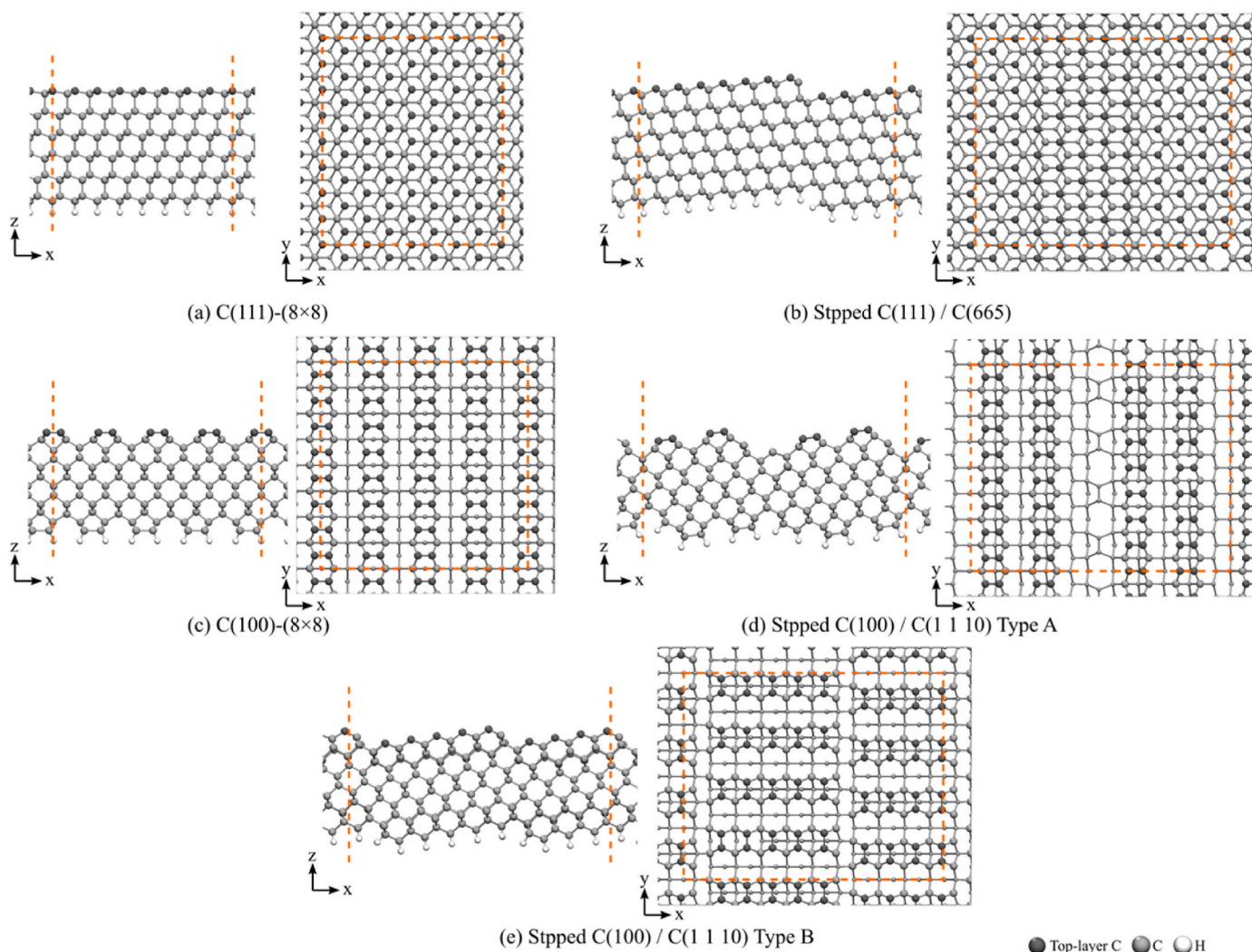
**Fig. 1.** Flat and stepped diamond (111) and (100) surface models used in production simulations. Dark grey spheres correspond to top-layer carbon atoms, while grey and white spheres correspond to the other carbon and hydrogen atoms, respectively.. (A color version of this figure can be viewed online.)

**Table 2**
Comparison of relevant surface properties calculated using 12-layer and 16-layer slab models.

| Properties | 12 Layers | 16 Layers |
|---|---|---|
| C(111) Reconstruction Energy (eV/atom) | −0.756 | −0.753 |
| C(111) Bilayer Exfoliation and Reconstruction Energy (eV/atom) | 0.125 | 0.131 |
| Surface Energy (eV/atom) | | |
| C(111) non-reconstructed | 2.161 | 2.159 |
| C(111) 2 × 1 reconstructed | 1.405 | 1.405 |
| C(100) 2 × 1 reconstructed | 2.410 | 2.410 |

positions are fixed during the simulations.

### 2.5. Machine learning analysis of the molecular dynamics data

The carbon atoms in graphite and diamond are $sp^2$- and $sp^3$-hybridized, respectively. An $sp^2$-hybridized atom has its s orbital hybridize with two p orbitals, resulting in a trigonal planar structure with three coordination. On the other hand, an $sp^3$-hybridized atom has its s orbital hybridize with three p orbitals, resulting in a tetragonal structure with four coordination. However, it is also possible to have 3-coordinated $sp^3$ hybridized atoms on the diamond surfaces ($sp^3$ with 1 dangling bond), which results in a slightly flattened tetragonal structure. In molecular dynamics simulations, the 3-coordinated and 4-coordinated atoms are typically assigned to $sp^2$-hybridized and $sp^3$-hybridized atoms, respectively [44]. However, since 3-coordinated atoms can either be $sp^2$- or $sp^3$-hybridized with a dangling bond, the classification is not trivial. The 3-coordinated $sp^3$ atoms could easily convert to 4-coordinated $sp^3$ when the dangling bond is saturated, hence, it should be properly distinguished from the 3-coordinated $sp^2$ atoms. To classify between the $sp^2$ and 3-coordinated $sp^3$ atoms, it is necessary to consider the bond lengths and the shape formed by the central atom and its nearest neighbors. To do this, we build a database of $sp^2$ and 3-coordinated $sp^3$ atoms with four features, namely the three bond lengths and the sum of the three bond angles, and either $sp^2$ or $sp^3$ as the target class. The $sp^2$ atoms came from graphite and graphene, while the 3-coordinated $sp^3$ atoms came from the first layer atoms of the diamond (111) and (100) surfaces. The coordinates of graphite, graphene, and the diamond (111) and (100) surfaces are perturbed randomly using uniform distribution to create new structures. The features are used as input to a neural network binary classifier model. The model has 3 hidden layers and an output layer where we used rectified linear unit (ReLU) and sigmoid activation function, respectively. The model is trained with binary cross-entropy loss function and adaptive moment estimation (Adam) optimizer as implemented in PyTorch machine learning framework [45].

## 3. Results and discussion

### 3.1. Graph neural network interatomic potential model for production simulations

The GNN interatomic potential that we used in the production simulations has been constructed from the database of 6302 structures, consisting of 452,656 atomic environments with 6302 total energy data corresponding to the structures and 1,357,968 force components. The energy and force root-mean-square errors (RMSE) of the test set are 0.003 eV/atom and 0.085 eV/Å, respectively. We subject the GNN-IP in the pre-production validation by simulating the C(111) and C(100) surfaces at increasing temperatures, up to 3600 K for the C(111) and 4400 K for the C(100). Comparison of the DFT and GNN energies and forces are shown in Fig. 2. The energy and force RMSEs of the pre-production validation set are 0.005 eV/atom and 0.128 eV/Å, respectively. The test and validation RMSEs that we obtained using GNN method are lower compared with the RMSE of the ML-IP for diamond and carbon materials constructed using Gaussian approximation potential (GAP) and neuro evolution potential (NEP) methods [46,47]. The sampled MD trajectories of the pre-production run have no extrapolated atomic environment feature vector with respect to the database. Next, we use the GNN-IP model to predict the equilibrium interatom separation in graphite and diamond crystals. The predicted interatom separation of both graphite and diamond agrees very well with DFT and experiment (Table 3). Finally, we used the GNN-IP model to calculate the surface energy of the diamond surfaces. The surface energies were calculated using the equation

$$\gamma = \frac{1}{2A}\left(2E_{slab1} - E_{slab2}\right) \tag{8}$$

where $E_{slab1}$ is the total energy of a 12-layer diamond slab with the bottom surface terminated by H-atoms, $E_{slab2}$ is the total energy of a 24-layer slab where the top and the bottom surfaces terminated by H-atoms, and A is the surface area of the slab [42]. The C(100) surface has higher surface energy compared to the C(111) surface, in good agreement with the DFT calculation (Table 4).

### 3.2. Thermal degradation of the flat and stepped diamond (111) and (100) surfaces

We investigated the thermal degradation of the C(111) and C(100) surfaces by performing MD simulations with constant heating rate of 10 K/ps. To analyze the results of MD simulations, we monitor the changes in the number of phase transformed atoms and their coordination. We define the phase transformed atoms as the atoms that move at least 0.8 Å

**Table 3**
GNN predicted interatom separation in graphite and diamond crystals compared with DFT and experiment.

| structure | GNN | DFT | experiment |
|---|---|---|---|
| graphite | 1.425 Å | 1.424 Å | 1.419 Å [48] |
| diamond | 1.544 Å | 1.546 Å [49] | 1.545 Å [50] |

**Table 4**
GNN predicted diamond surface energies compared with DFT.

| | GNN | DFT (this study) | DFT (Ref [51]) |
|---|---|---|---|
| C(111)-(2 × 1) | 3.42 J/m² (1.18 eV/ atom) | 4.09 J/m² (1.41 eV/ atom) | 4.06 J/m² (1.37 eV/ atom) |
| C(100)-(2 × 1) | 5.07 J/m² (2.02 eV/ atom) | 6.05 J/m² (2.41 eV/ atom) | 5.71 J/m² (2.2 eV/ atom) |

away from their initial positions. The cutoff for the calculation of the coordination number is 2.0 Å. The simulation is carried out until about four layers of the surface has been phase transformed or thermally degraded.

We start with the simulation of the C(111) surface (Fig. 3a). At t = 52 ps (T ~ 520K), a number of atoms start to undergo phase transformation. The number of phase transformed atoms is almost unchanged up to t = 260 ps (T ~ 2600K), suggesting that this phase is at least meta-stable within these temperature range. Upon examination of the snapshot at t = 60 ps, the phase transformation is characterized by the (2 × 1) π-bonding reconstruction of the C(111) surface (Fig. 4a). We investigated the temperature dependence of the π-bonding reconstruction by first performing constant heating rate simulation from 0 K up to a target temperature, and then keeping the simulation temperature constant. When the target temperature is 500 K, the π-bonding reconstruction occurred within 4.5 ps. When the target temperature is lowered to 400 K and 300 K, the time required to reconstruct increased to 50.0 ps and 68.3 ps, respectively. We also simulated at 280 K for 500 ps but did not observe π-bonding reconstruction. The results suggest that the C(111) (2 × 1) π-bonding reconstruction is a thermally activated process and agrees with earlier theoretical studies using first principles calculations [42,52]. The thermal degradation of the surface occurs from t = 285 ps (T ~ 2850K) as shown by the sharp increase of 3-coordinated phase transformed atoms. The thermal degradation of the C(111) surface occurs through bilayer exfoliation, which starts with the breaking of bonds between the second- and third-layer C atoms. This bond breaking mechanism is similar to the cleaving of the C(111) surface which breaks one bond per atom. When attached to the surface, the top bilayer has buckled structure with the characteristic tetrahedral geometry of diamond. After it has been detached, the top bilayer is exfoliated, and forms
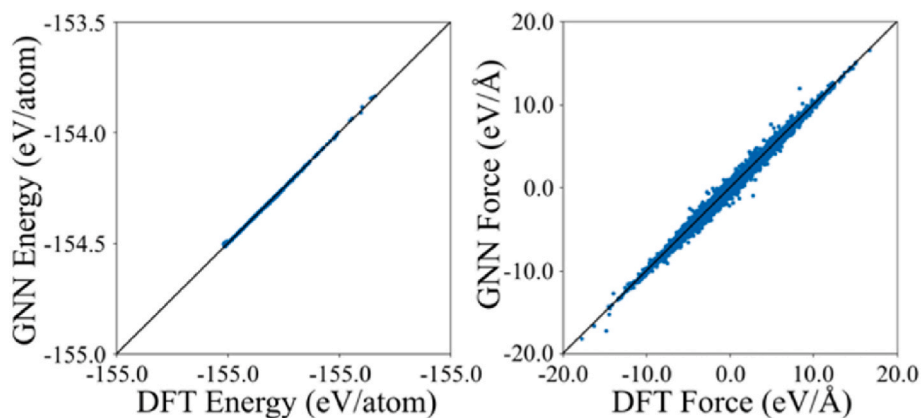


**Fig. 2.** Comparison of the DFT and GNN energies and forces for the pre-production validation set, with energy and force RMSEs of 0.005 eV/atom and 0.128 eV/Å, respectively.
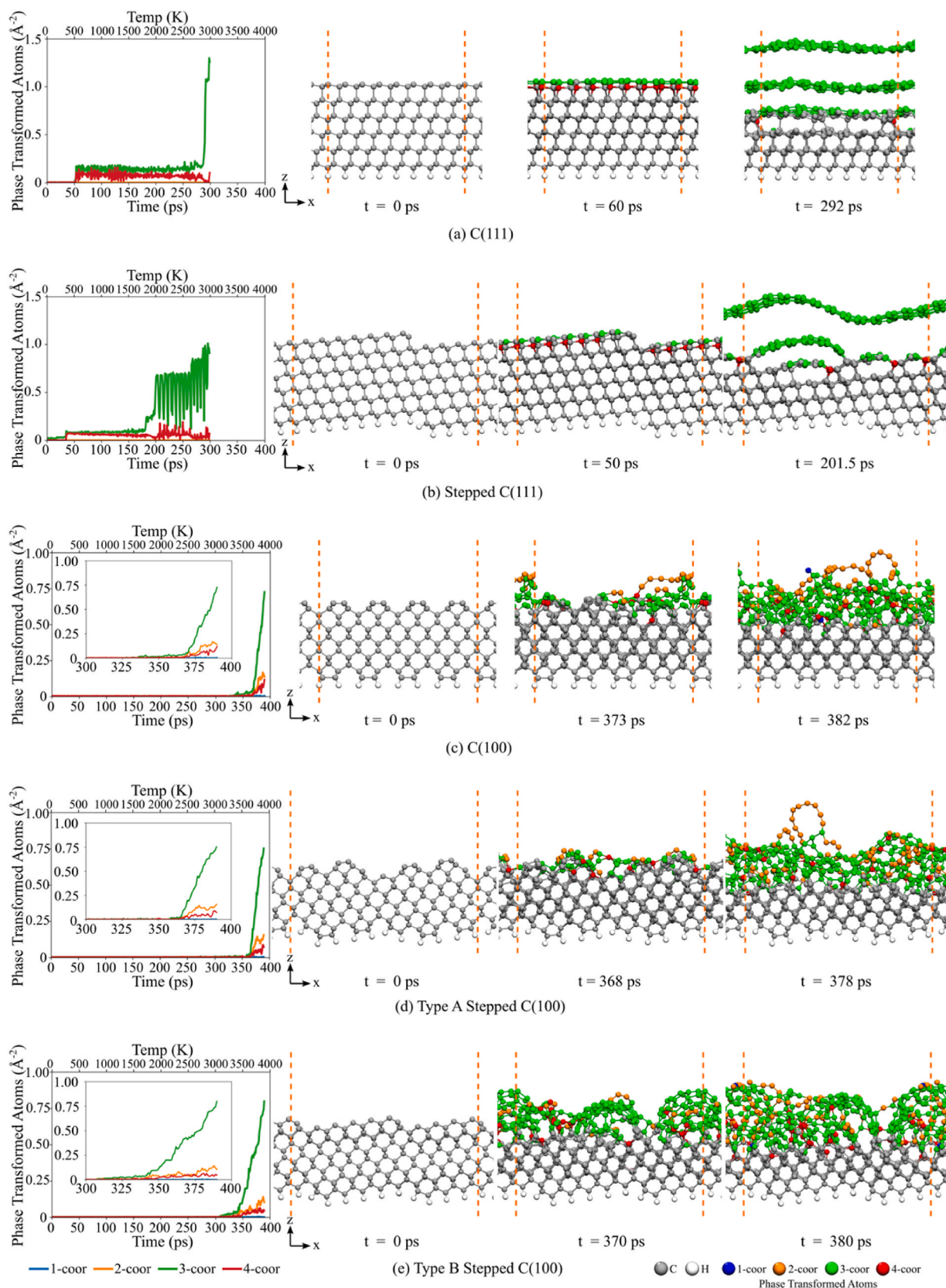
**Fig. 3.** The results of MD simulations of the diamond surfaces at a constant heating rate of 10 K/ps. For each surface model, the number of phase transformed atoms per Å² during the simulation is shown, with blue, orange, green, and red lines corresponding to 1-, 2-, 3-, and 4-coordinated atoms, respectively. Snapshots of the MD simulation at selected timesteps are also shown with blue, orange, green, and red spheres corresponding to 1-, 2-, 3-, and 4-coordinated phase transformed atoms, respectively. Grey and white spheres correspond to non-phase transformed carbon and hydrogen atoms, respectively.. (A color version of this figure can be viewed online.)
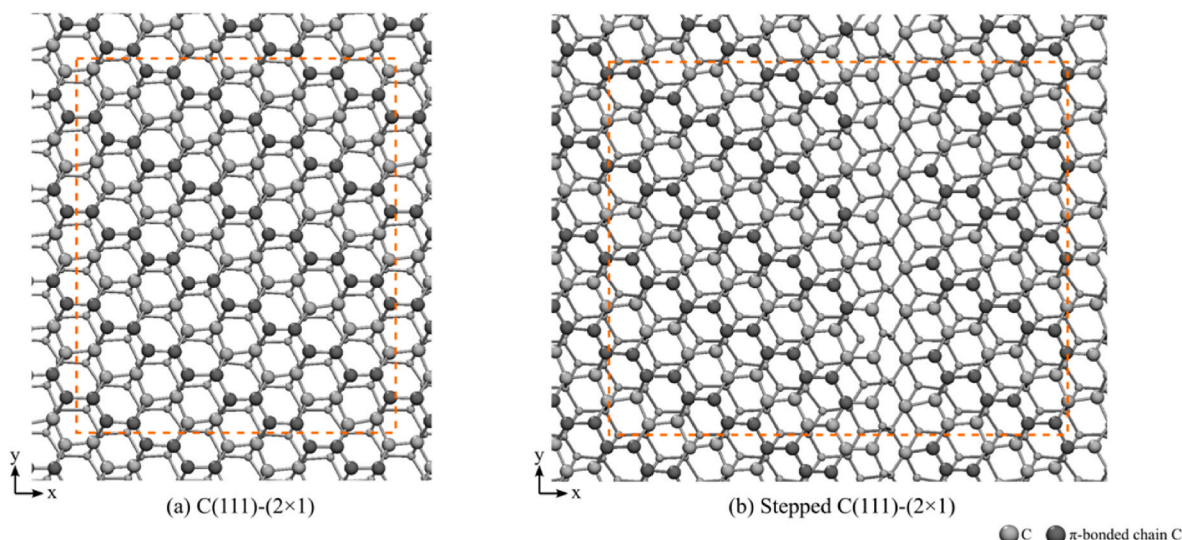
**Fig. 4.** Snapshots of (2 × 1) π-bonded reconstruction of the (a) C(111) surface (t = 60 ps, T ~ 600K) and (b) stepped C(111) surface (t = 50 ps, T ~ 500K). Dark grey spheres correspond to π-bonded carbon atoms while grey spheres correspond to other carbon atoms.. (A color version of this figure can be viewed online.)

corrugated graphene-like sheet where the C atoms are all 3-coordinated and form 6-membered rings. The snapshot at t = 292 ps shows a thermally degraded C(111) surface with two exfoliated bilayers. To estimate the activation energy of the bilayer exfoliation, we performed static DFT calculations and nudged elastic band reaction path search [53]. The activation energy is 0.758 eV/atom (2.199 J/m²). Using the GNN-IP, the calculated energy barrier is 0.717 eV/atom (2.081 J/m²) which shows good agreement with DFT.

Fig. 3b shows the results of the simulation of the stepped C(111) surface. The (2 × 1) π-bonding reconstruction starts at an earlier timestep of t = 35 ps (T ~ 350K). The completed reconstruction is shown in the snapshot at t = 50 ps. The π-bonding chain is formed at an angle of 60° across the steps (Fig. 4b). The thermal degradation of the stepped C(111) surface starts to occur at an earlier timestep of t = 181 ps (T ~ 1810K) compared with the flat C(111) surface. This difference is caused by the dangling bonds already present on the second-layer atoms at the step edges which promotes bilayer exfoliation. The snapshot at t = 201.5 ps shows a thermally degraded stepped C(111) surface with the top two terraces that have been exfoliated and have combined into a single 3-coordinated C atom rippled sheet that forms graphene-like 6-membered rings. The remaining terraces contains sections with 2 × 1 reconstructed atoms and partially exfoliated C atom sheets.

Next, we discuss the results of the simulation of the C(100) surface (Fig. 3c). The thermal degradation of the surface starts at a much later timestep of t = 368 ps (T ~ 3680K) compared to the C(111) surface. This shows that the C(100) surface has higher thermal degradation resistance compared to the C(111) surface. As can be seen from the MD snapshots at t = 373 ps and t = 382 ps, unlike the C(111) surface, the thermal degradation of the C(100) surface does not proceed through the exfoliation of the top bilayer. Exfoliation of the top bilayer of the C(100) surface requires synchronous breaking of two bonds per atom which is a more stringent requirement compared to the one bond per atom requirement of cleaving the top bilayer on the C(111) surface. Instead of bilayer exfoliation, the C(100) surface degrade by breaking bonds between layers and the degradation proceeds through a small cluster of phase transformed atoms that grows until it covers the entire surface. The thermal degradation causes the surface to expand, which supports the observation in the laser ablation of diamond [54]. The phase transformed atoms consist of 2-, 3-, and 4-coordinated C atoms. Having 2-coordinated carbon chains shows that there are more broken bonds per atom in the thermal degradation of the C(100) surface compared to the C(111) surface.

Fig. 3d and e show the results of the simulations of the Type A and Type B stepped C(100) surfaces. The main difference between the two stepped surface models is the absence or presence of dangling bonds on the second-layer atoms on the step edges. When the C-dimer bond is normal to the step edge (Type A), there is no dangling bond on the second-layer atoms at step edge. But when the C-dimer bond is parallel to the step edge (Type B), there is 1 dangling bond per second-layer atom at the step edge. This leads to the difference in the thermal degradation mechanism of the two stepped surface models. For the Type A stepped C(100) surface, the thermal degradation of the surface starts at t = 350 ps (T ~ 3500 K) which is just slightly lower compared to the flat C(100) surface. Similar to the flat C(100) surface, the thermal degradation starts with disordered clusters of 2-, 3-, and 4-coordinated phase transformed C atoms and grows until it covers the step terrace. In contrast, for the Type B stepped C(100) surface, the thermal degradation of the surface occurs at a much earlier timestep of t = 307 ps (T ~ 3070K). Also, the rate of increase of the phase transitioned atoms is slower compared to the flat C(100) surface. Moreover, the thermally degraded structure is noticeably different. The number of thermally degraded atoms with 2-coordination is lesser, while 3-coordinated atoms with short-range order are observed. The thermal degradation starts with the formation of cylindrical and dome-like structures at the step edges. The cylindrical structure consists of 3-coordinated atoms that form 6-membered rings similar to graphene, while the dome-like structures consist of 3-coordinated atoms that form 5- and 6-membered rings similar to fullerenes. As the thermal degradation progresses, the cylindrical and dome-like structures combine and become more disordered.

We also perform same simulations at a faster heating rate of 200 K/ps. The predicted thermal degradation temperature is higher compared to the ones predicted in the slower heating rate simulation (Table 5). For instance, at slower heating rate of 10 K/ps, the graphitization starts at

**Table 5**
Comparison of the thermal degradation temperatures of the diamond surfaces for slow (10 K/ps) and fast (200 K/ps) heating rates.

| structure | thermal degradation temperature (K) | |
|---|---|---|
| | slower heating rate | faster heating rate |
| C(111) | 2850 | 3240 |
| C(111) stepped | 1810 | 2840 |
| C(100) | 3680 | 4050 |
| Stepped C(100) Type A | 3500 | 3900 |
| Stepped C(100) Type A | 3070 | 3640 |

1810 K for the stepped C(111) surface which is close to the temperatures in the experiment, in which the graphitization of diamond microcrystals occurs within a few minutes when heated at 1600 $^\circ C$ (1873 K) which starts from the edges and the C(111) facet [15]. At faster heating rate of 200 K/ps, the predicted graphitization temperature for the same surface is higher (2840 K). Next, we calculated the thermal degradation of the flat and stepped C(111) surface for increasing heating rates and plotted thermal degradation temperatures (Fig. 5). The graph shows that the thermal degradation temperature converges at 10K/ps. Therefore, while 10 K/ps is still much faster compared to the one used in the experiment (15 $^\circ C$/min) [15], it is still possible to predict realistic thermal degradation temperature with this value of heating rate.

### 3.3. Hybridization of carbon atoms on the thermally degraded diamond surfaces

To gain further insights, we classify the phase transformed atoms of the thermally degraded surfaces according to their hybridization. The 1- and 2-coordinated atoms are classified as $sp^1$-hybridized, and the 4-coordinated atoms are classified as $sp^3$-hybridized. The 3-coordinated atoms can either be $sp^2$ hybridized or $sp^3$ hybridized with a dangling bond, depending on the bond lengths and bond angles. To classify the 3-coordinated atoms whether they have $sp^2$ or $sp^3$ character, we constructed a neural network binary classifier model with bond lengths and bond angles as input features. The details of this binary classifier model are discussed in the methodology section. The classified structures of thermally degraded surfaces are shown in Fig. 6 with the calculated percent composition of each hybridization type for each structure. In addition, structure analysis using the coordination number is also presented. While the coordination analysis is a good metric to contrast between the amount of 1-, 2-, and 4-coordinated thermally degraded atoms on the flat and stepped C(111) and C(100) surfaces, it gives limited insight in differentiating between the type of thermally degraded 3-coordinated atoms on the surfaces. For this task, the hybridization analysis allows further elucidation.

The exfoliated sheet on the thermally degraded C(111) surface contains $sp^2$ and 3-coordinated $sp^3$ hybridized atoms forming 6-membered rings (Fig. 6a). The corrugation is caused by the compressive stress due to the mismatch between the lattice parameter of the C(111) surface and graphene, which prevents the 3-coordinated $sp^3$ atoms to fully flatten and change into $sp^2$ hybridization. In physical systems, the exfoliated sheet will likely become purely $sp^2$-hybridized when the compressive stress is lifted. Similarly, the exfoliated rippled sheet and the partially exfoliated sublayer of the stepped C(111) surface contain C atoms in 6-membered rings with both $sp^2$ and $sp^3$ character (Fig. 6b).

In contrast, the thermally degraded C(100) surface contains $sp^1$

hybridized carbon chains and an amorphous network of $sp^2$-hybridized and 3- and 4-coordinated $sp^3$-hybridized C atoms (Fig. 6c). In physical systems, the 3-coordinated $sp^3$-hybridized C atoms can either form bond with other atoms to saturate the dangling bond or flatten to change into $sp^2$ hybridization upon annealing. Also, as argued by O'Bannon et al. the $sp^1$-hybridized carbon will transform into zigzag chain and combine to form into more stable $sp^2$-hybridized carbon [23]. The thermally degraded structure on the Type A stepped C(100) surface is similar to the flat C(100) surface (Fig. 6d). In contrast, the Type B stepped C(100) surface has noticeably less $sp^1$ hybridized carbon chains (Fig. 6e). Also, unlike in the flat and the Type A stepped C(100) surface, the $sp^2$ and 3-coordinated $sp^3$ structures on the Type B stepped C(100) surface have short range order, which form into graphene-like and semi fullerene-like structures with 5- and 6-membered rings. The 3-coordinated $sp^3$-hybridized carbon atoms in these rings will likely flatten upon annealing. The formation of half fullerene-like structure supports the experimental observation that fullerene can form during CVD growth of diamond and that diamond can be formed from fullerene [55,56].

## 4. Conclusions

The MLMD simulations using GNN-IP reveal the origins of the surface facet dependence in the thermal degradation of the C(111) and C(100) surfaces. The C(111) surface thermally degrade through the exfoliation of the top bilayer which forms into highly ordered 6-membered rings. On the other hand, the exfoliation of the top bilayer does not occur on the C(100) surface since it requires the breaking of two bonds per atom which is a more stringent requirement compared to the one bond per atom requirement of exfoliating the top bilayer on the C(111) surface. As a result, the C(111) surface is more susceptible to thermal degradation compared to the C(100) surface. The thermally degraded C(100) atoms consist of 2-coordinated carbon chains and 3-coordinated amorphous carbon. We also investigated the thermal degradation of the stepped diamond surfaces. In general, the stepped surfaces are more susceptible to thermal degradation compared to corresponding flat surfaces. The dangling bonds of atoms on the step edge facilitate bond breaking between the surface and sublayer atoms and lead to lower thermal degradation temperature.

Since thermal degradation is enhanced by the presence of dangling bonds, we propose that terminating the dangling bonds at the steps could prevent the premature wear of diamond tools. Recently, diamond tool wear suppression when cutting steel has been demonstrated in vibration cutting [57,58]. The proposed mechanism is that the steel oxidizes when exposed to air, which prevents the direct contact and chemical reaction between the steel and the diamond tool. We propose a secondary mechanism where the graphitization is suppressed due to the termination of diamond dangling bonds by oxygen atoms, particularly in the flank face of the tool.

Moreover, we found that through thermally induced process, the top bilayer of the C(111) surface can be exfoliated without significant damage to the sublayer atoms. This mechanism could be used in the design of novel diamond polishing methods. For instance, the dangling bond on the edges make asperities more susceptible to graphitization. Therefore, preheating the surface prior to polishing will selectively graphitize the asperities and could potentially improve the material removal rate and the quality of the polished surface.

Finally, our simulations show the atomistic mechanism of the production of graphene directly from the diamond surface which has been proposed in the past using metal catalysts [59,60]. There is a growing interest in the graphene-on-diamond electronic devices which have superior electronic and thermal properties compared to conventional graphene-on-silicon devices [61–63]. Our results suggest that the C(111) surface is more likely to produce better quality graphene, since the $sp^2$ atoms mainly form 6-membered rings, resulting in a planar surface. On the C(100) surface, particularly on the Type B stepped surface edges, the $sp^2$ atoms also form 5 membered rings aside from the 6-membered
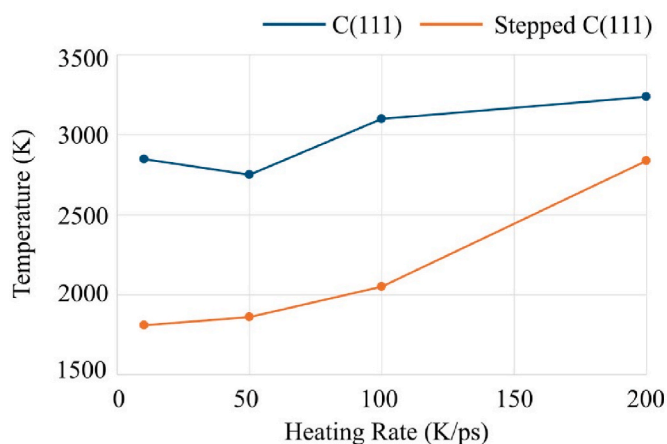


**Fig. 5.** Variation of thermal degradation temperature with heating rate for the flat and stepped C(111) surfaces.
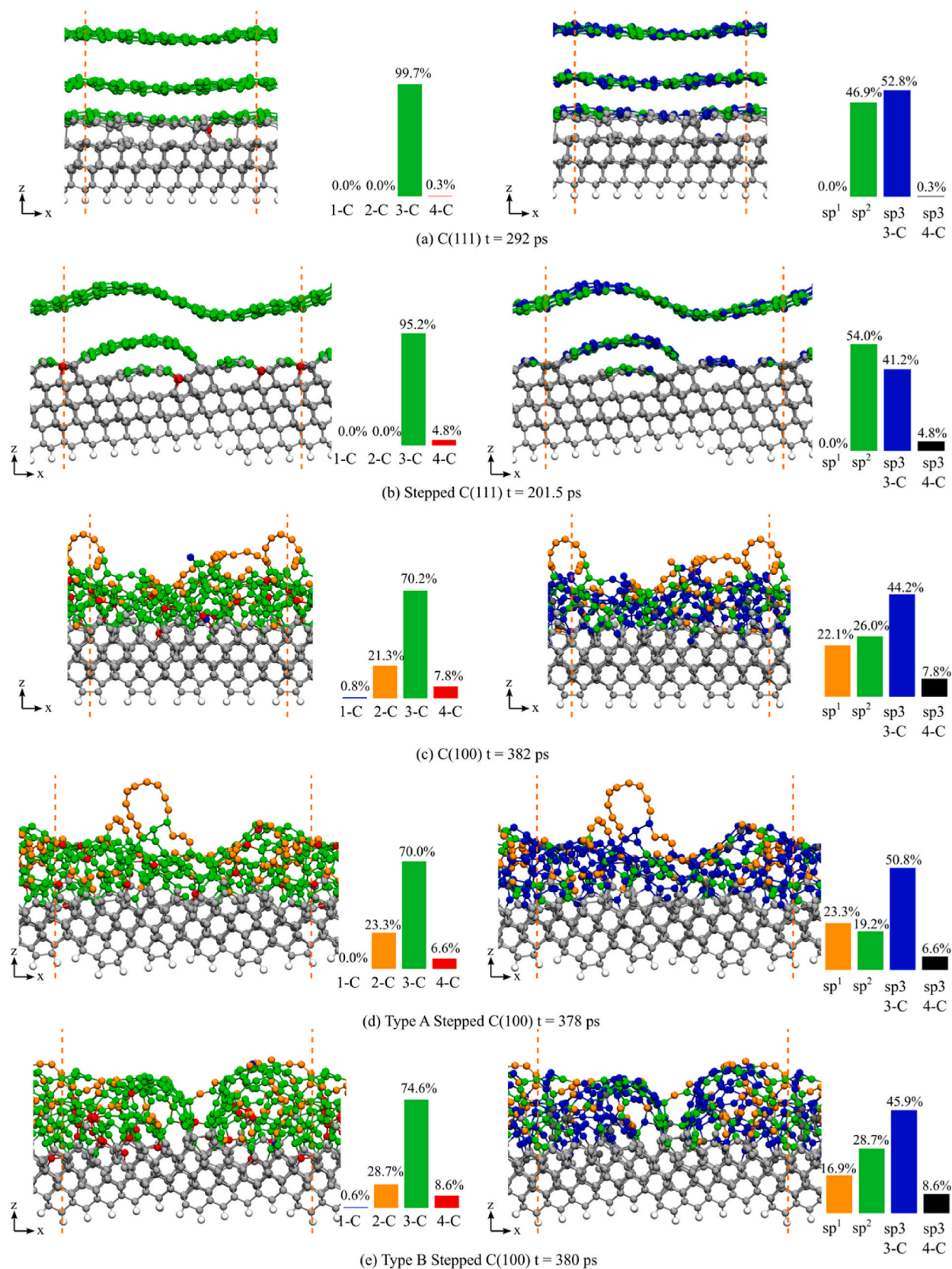
**Fig. 6.** Coordination (left) and hybridization (right) analysis of carbon atoms on the thermally degraded diamond surfaces. Snapshots of the MD simulation at selected timesteps are shown with blue, orange, green, and red spheres corresponding to 1-coordinated, 2-coordinated, 3-coordinated, and 4-coordinated C atoms (left) and orange, green, blue, and black spheres corresponding to $sp^1$, $sp^2$, 3-coordinated $sp^3$, or 4-coordinated $sp^3$ hybridized C atoms (right). Grey and white spheres correspond to non-phase transformed diamond and hydrogen atoms. The percent composition of each type of coordination and hybridization for each structure is calculated.. (A color version of this figure can be viewed online.)

rings, which will result on a buckled and rather less ordered graphitic structure.

## CRediT authorship contribution statement

**John Isaac G. Enriquez:** Writing – original draft, Visualization, Software, Investigation, Formal analysis. **Harry Handoko Halim:** Writing – review & editing. **Takahiro Yamasaki:** Supervision, Project administration, Conceptualization. **Masato Michiuchi:** Supervision, Project administration, Conceptualization. **Kouji Inagaki:** Writing – review & editing, Software, Methodology, Conceptualization. **Masaaki Geshi:** Methodology, Conceptualization. **Ikutaro Hamada:** Writing – review & editing, Software. **Yoshitada Morikawa:** Writing – review & editing, Supervision, Software, Project administration, Methodology, Funding acquisition, Conceptualization.

## Declaration of competing interest

The authors declare that they have no known competing financial interests or personal relationships that could have appeared to influence the work reported in this paper.

## Appendix A. Supplementary data

Supplementary data to this article can be found online at https://doi.org/10.1016/j.carbon.2024.119223.

## References

[1] D.E. Brehl, T.A. Dow, Review of vibration-assisted machining, Precis. Eng. 32 (2008) 153–172, https://doi.org/10.1016/j.precisioneng.2007.08.003.

[2] C.J.H. Wort, R.S. Balmer, Diamond as an electronic material, Mater. Today 11 (2008) 22–28, https://doi.org/10.1016/S1369-7021(07)70349-8.

[3] D. Araujo, M. Suzuki, F. Lloret, G. Alba, P. Villar, Diamond for electronics: materials, processing and devices, Materials 14 (2021) 7081, https://doi.org/10.3390/ma14227081.

[4] I. Aharonovich, A.D. Greentree, S. Prawer, Diamond photonics, Nature Photon 5 (2011) 397–405, https://doi.org/10.1038/nphoton.2011.54.

[5] S. Prawer, A.D. Greentree, Diamond for quantum computing, Science 320 (2008) 1601–1602, https://doi.org/10.1126/science.1158340.

[6] M. Seal, Graphitization and Plastic Deformation of diamond, Nature 182 (1958) 1264–1267, https://doi.org/10.1038/1821264a0.

[7] X. Yan, J. Wei, J. Guo, C. Hua, J. Liu, L. Chen, L. Hei, C. Li, Mechanism of graphitization and optical degradation of CVD diamond films by rapid heating treatment, Diam. Relat. Mater. 73 (2017) 39–46, https://doi.org/10.1016/j.diamond.2016.11.010.

[8] B. Ali, I.V. Litvinyuk, M. Rybachuk, Femtosecond laser micromachining of diamond: Current research status, applications and challenges, Carbon 179 (2021) 209–226, https://doi.org/10.1016/j.carbon.2021.04.025.

[9] A.G. Thornton, J. Wilks, The wear of diamond tools turning mild steel, Wear 65 (1980) 67–74, https://doi.org/10.1016/0043-1648(80)90009-5.

[10] J. Wang, L. Wan, J. Chen, J. Yan, Anisotropy of synthetic diamond in catalytic etching using iron powder, Appl. Surf. Sci. 346 (2015) 388–393, https://doi.org/10.1016/j.apsusc.2015.04.022.

[11] N. Liu, K. Sugimoto, N. Yoshitaka, H. Yamada, R. Sun, K. Kawai, K. Arima, K. Yamamura, Effects of polishing pressure and sliding speed on the material removal mechanism of single crystal diamond in plasma-assisted polishing, Diam.

[12] R.P. Mildren, J.E. Downes, J.D. Brown, B.F. Johnston, E. Granados, D.J. Spence, A. Lehmann, L. Weston, A. Bramble, Characteristics of 2-photon ultraviolet laser etching of diamond, Opt. Mater. Express, OME 1 (2011) 576–585, https://doi.org/10.1364/OME.1.000576.

[13] X. Yan, J. Wei, K. An, J. Liu, L. Chen, X. Zhang, C. Li, Graphitization of CVD diamond grain boundaries during transient heat treatment, Diam. Relat. Mater. 116 (2021) 108433, https://doi.org/10.1016/j.diamond.2021.108433.

[14] 4 - Key technologies for device fabrications and materials characterizations, in: S. Koizumi, H. Umezawa, J. Pernot, M. Suzuki (Eds.), Power Electronics Device Applications of Diamond Semiconductors, Woodhead Publishing, 2018, pp. 219–294, https://doi.org/10.1016/B978-0-08-102183-5.00004-2.

[15] B.B. Bokhonov, D.V. Dudina, M.R. Sharafutdinov, Graphitization of synthetic diamond crystals: a morphological study, Diam. Relat. Mater. 118 (2021) 108563, https://doi.org/10.1016/j.diamond.2021.108563.

[16] G. Kern, J. Hafner, Ab initio molecular-dynamics studies of the graphitization of flat and stepped diamond (111) surfaces, Phys. Rev. B 58 (1998) 13167–13175, https://doi.org/10.1103/PhysRevB.58.13167.

[17] M. Seal, Graphitization of diamond, Nature 185 (1960) 522–523, https://doi.org/10.1038/185522a0.

[18] V.R. Howes, The graphitization of diamond, Proc. Phys. Soc. 80 (1962) 648, https://doi.org/10.1088/0370-1328/80/3/310.

[19] C. de Tomas, I. Suarez-Martinez, N.A. Marks, Graphitization of amorphous carbons: a comparative study of interatomic potentials, Carbon 109 (2016) 681–693, https://doi.org/10.1016/j.carbon.2016.08.024.

[20] Q. Bai, Z. Wang, Y. Guo, J. Chen, Y. Shang, Graphitization behavior of single crystal diamond for the application in Nano-metric cutting, Curr. Nanosci. 14 (2018) 377–383, https://doi.org/10.2174/1573413714666180517080721.

[21] A. Bródka, T.W. Zerda, A. Burian, Graphitization of small diamond cluster — molecular dynamics simulation, Diam. Relat. Mater. 15 (2006) 1818–1821, https://doi.org/10.1016/j.diamond.2006.06.002.

[22] L. Nistor, V. Ralchenko, I. Vlasov, A. Khomich, R. Khmelnitskii, P. Potapov, J. Van Landuyt, Formation of amorphous carbon and graphite in CVD diamond upon annealing: a HREM, EELS, Raman and optical study, Phys. Status Solidi 186 (2001) 207–214, https://doi.org/10.1002/1521-396X(200108)186:2<207::AID-PSSA207>3.0.CO;2-U.

[23] E. O'Bannon, G. Xia, F. Shi, R. Wirth, A. King, L. Dobrzhinetskaya, The transformation of diamond to graphite: experiments reveal the presence of an intermediate linear carbon phase, Diam. Relat. Mater. 108 (2020) 107876, https://doi.org/10.1016/j.diamond.2020.107876.

[24] S. Batzner, A. Musaelian, L. Sun, M. Geiger, J.P. Mailoa, M. Kornbluth, N. Molinari, T.E. Smidt, B. Kozinsky, E(3)-equivariant graph neural networks for data-efficient and accurate interatomic potentials, Nat. Commun. 13 (2022) 2453, https://doi.org/10.1038/s41467-022-29939-5.

[25] J. Behler, M. Parrinello, Generalized neural-network Representation of high-Dimensional potential-energy surfaces, Phys. Rev. Lett. 98 (2007) 146401, https://doi.org/10.1103/PhysRevLett.98.146401.

[26] R. Goeminne, L. Vanduyfhuys, V. Van Speybroeck, T. Verstraelen, DFT-quality adsorption simulations in metal–organic frameworks enabled by machine learning potentials, J. Chem. Theor. Comput. 19 (2023) 6313–6325, https://doi.org/10.1021/acs.jctc.3c00495.

[27] R.J. Bunting, F. Wodaczek, T. Torabi, B. Cheng, Reactivity of single-atom alloy nanoparticles: modeling the dehydrogenation of Propane, J. Am. Chem. Soc. 145 (2023) 14894–14902, https://doi.org/10.1021/jacs.3c04030.

[28] M. Ghim, Y.-J. Choi, S.-H. Jhi, Lattice thermal conductivity of cubic GeTe with vacancy defects, Phys. Rev. B 107 (2023) 184301, https://doi.org/10.1103/PhysRevB.107.184301.

[29] S. Baker, J. Pagotto, T.T. Duignan, A.J. Page, High-throughput aqueous electrolyte structure prediction using IonSolvR and equivariant graph neural network potentials, J. Phys. Chem. Lett. 14 (2023) 9508–9515, https://doi.org/10.1021/acs.jpclett.3c01783.

[30] J. Gilmer, S.S. Schoenholz, P.F. Riley, O. Vinyals, G.E. Dahl, Neural Message Passing for Quantum Chemistry, 2017, https://doi.org/10.48550/ARXIV.1704.01212.

[31] W. Kohn, L.J. Sham, Self-Consistent equations including exchange and correlation effects, Phys. Rev. 140 (1965) A1133–A1138, https://doi.org/10.1103/PhysRev.140.A1133.

[32] STATE Code, (n.d.). http://www-cp.prec.eng.osaka-u.ac.jp/puki_state/(accessed May 13, 2023).

[33] Y. Morikawa, H. Ishii, K. Seki, Theoretical study of n-alkane adsorption on metal surfaces, Phys. Rev. B 69 (2004) 041403, https://doi.org/10.1103/PhysRevB.69.041403.

[34] J.P. Perdew, K. Burke, M. Ernzerhof, Generalized gradient approximation made Simple, Phys. Rev. Lett. 77 (1996) 3865–3868, https://doi.org/10.1103/PhysRevLett.77.3865.

[35] S. Grimme, Semiempirical GGA-type density functional constructed with a long-range dispersion correction, J. Comput. Chem. 27 (2006) 1787–1799, https://doi.org/10.1002/jcc.20495.

[36] D. Vanderbilt, Soft self-consistent pseudopotentials in a generalized eigenvalue formalism, Phys. Rev. B 41 (1990) 7892–7895, https://doi.org/10.1103/PhysRevB.41.7892.

[37] H.J. Monkhorst, J.D. Pack, Special points for Brillouin-zone integrations, Phys. Rev. B 13 (1976) 5188–5192, https://doi.org/10.1103/PhysRevB.13.5188.

[38] A.A. Correa, S.A. Bonev, G. Galli, Carbon under extreme conditions: phase boundaries and electronic properties from first-principles theory, Proc. Natl. Acad. Sci. U.S.A. 103 (2006) 1204–1208, https://doi.org/10.1073/pnas.0510489103.

[39] J.T. Willman, K. Nguyen-Cong, A.S. Williams, A.B. Belonoshko, S.G. Moore, A. P. Thompson, M.A. Wood, I.I. Oleynik, Machine learning interatomic potential for simulations of carbon at extreme conditions, Phys. Rev. B 106 (2022), https://doi.org/10.1103/PhysRevB.106.L180101. L180101.

[40] A.P. Thompson, H.M. Aktulga, R. Berger, D.S. Bolintineanu, W.M. Brown, P. S. Crozier, P.J. In 'T Veld, A. Kohlmeyer, S.G. Moore, T.D. Nguyen, R. Shan, M. J. Stevens, J. Tranchida, C. Trott, S.J. Plimpton, LAMMPS - a flexible simulation tool for particle-based materials modeling at the atomic, meso, and continuum scales, Comput. Phys. Commun. 271 (2022) 108171, https://doi.org/10.1016/j.cpc.2021.108171.

[41] W.G. Hoover, Canonical dynamics: equilibrium phase-space distributions, Phys. Rev. A 31 (1985) 1695–1697, https://doi.org/10.1103/PhysRevA.31.1695.

[42] J.I.G. Enriquez, T. Yamasaki, M. Michiuchi, K. Inagaki, M. Geshi, I. Hamada, Y. Morikawa, Origin of the surface facet dependence in the Oxidative etching of the diamond (111) and (100) surfaces from first-principles calculations, J. Phys. Chem. C 128 (2024) 6294–6308, https://doi.org/10.1021/acs.jpcc.3c08378.

[43] D.J. Chadi, Stabilities of single-layer and bilayer steps on Si(001) surfaces, Phys. Rev. Lett. 59 (1987) 1691–1694, https://doi.org/10.1103/PhysRevLett.59.1691.

[44] T. Ma, Y.-Z. Hu, Y. Wang, X. Li, Microstructural and stress properties of ultrathin diamondlike carbon films during growth: molecular dynamics simulations, Phys. Rev. B 75 (2007) 035425, https://doi.org/10.1103/PhysRevB.75.035425.

[45] A. Paszke, S. Gross, F. Massa, A. Lerer, J. Bradbury, G. Chanan, T. Killeen, Z. Lin, N. Gimelshein, L. Antiga, A. Desmaison, A. Köpf, E. Yang, Z. DeVito, M. Raison, A. Tejani, S. Chilamkurthy, B. Steiner, L. Fang, J. Bai, S. Chintala, PyTorch: an Imperative Style, high-performance deep learning library. https://doi.org/10.48550/ARXIV.1912.01703, 2019.

[46] P. Rowe, V.L. Deringer, P. Gasparotto, G. Csányi, A. Michaelides, An accurate and transferable machine learning potential for carbon, J. Chem. Phys. 153 (2020) 034702, https://doi.org/10.1063/5.0005084.

[47] Y. Li, J.-W. Jiang, Vacancy defects impede the transition from peapods to diamond: a neuroevolution machine learning study, Phys. Chem. Chem. Phys. 25 (2023) 25629–25638, https://doi.org/10.1039/D3CP03862A.

[48] C. Kittel, Introduction to Solid State Physics, seventh ed., Wiley, New York, 1996.

[49] J.I. Enriquez, F. Muttaqien, M. Michiuchi, K. Inagaki, M. Geshi, I. Hamada, Y. Morikawa, Oxidative etching mechanism of the diamond (100) surface, Carbon 174 (2021) 36–51, https://doi.org/10.1016/j.carbon.2020.11.057.

[50] S. Shikata, T. Tanno, T. Teraji, H. Kanda, T. Yamada, J. Kushibiki, Precise measurements of diamond lattice constant using Bond method, Jpn. J. Appl. Phys. 57 (2018) 111301, https://doi.org/10.7567/JJAP.57.111301.

[51] A.A. Stekolnikov, J. Furthmüller, F. Bechstedt, Absolute surface energies of group-IV semiconductors: dependence on orientation and reconstruction, Phys. Rev. B 65 (2002) 115318, https://doi.org/10.1103/PhysRevB.65.115318.

[52] D. Petrini, K. Larsson, Theoretical study of the thermodynamic and kinetic aspects of terminated (111) diamond surfaces, J. Phys. Chem. C 112 (2008) 3018–3026, https://doi.org/10.1021/jp709625a.

[53] G. Henkelman, B.P. Uberuaga, H. Jónsson, A climbing image nudged elastic band method for finding saddle points and minimum energy paths, J. Chem. Phys. 113 (2000) 9901–9904, https://doi.org/10.1063/1.1329672.

[54] M.S. Komlenok, V.V. Kononenko, V.G. Ralchenko, S.M. Pimenov, V.I. Konov, Laser induced nanoablation of diamond materials, Phys. Procedia 12 (2011) 37–45, https://doi.org/10.1016/j.phpro.2011.03.103.

[55] L. Chow, H. Wang, S. Kleckley, T.K. Daly, P.R. Buseck, Fullerene formation during production of chemical vapor deposited diamond, Appl. Phys. Lett. 66 (1995) 430–432, https://doi.org/10.1063/1.114046.

[56] V.V. Brazhkin, A.G. Lyapin, S.V. Popova, YuA. Klyuev, A.M. Naletov, Mechanical properties of the 3D polymerized, sp2–sp3 amorphous, and diamond-plus-graphite nanocomposite carbon phases prepared from C60 under high pressure, J. Appl. Phys. 84 (1998) 219–226, https://doi.org/10.1063/1.368021.

[57] X. Zhang, H. Deng, K. Liu, Oxygen-shielded ultrasonic vibration cutting to suppress the chemical wear of diamond tools, CIRP Annals 68 (2019) 69–72, https://doi.org/10.1016/j.cirp.2019.04.026.

[58] X. Zhang, R. Huang, Y. Wang, K. Liu, H. Deng, D.W.K. Neo, Suppression of diamond tool wear with sub-millisecond oxidation in ultrasonic vibration cutting of steel, J. Mater. Process. Technol. 299 (2022) 117320, https://doi.org/10.1016/j.jmatprotec.2021.117320.

[59] K. Ueda, S. Aichi, H. Asano, Direct formation of graphene layers on diamond by high-temperature annealing with a Cu catalyst, Diam. Relat. Mater. 63 (2016) 148–152, https://doi.org/10.1016/j.diamond.2015.10.021.

[60] N. Suntornwipat, A. Aitkulova, V. Djurberg, S. Majdi, Rapid direct growth of graphene on single-crystalline diamond using nickel as catalyst, Thin Solid Films 770 (2023) 139766, https://doi.org/10.1016/j.tsf.2023.139766.

[61] J. Yu, G. Liu, A.V. Sumant, V. Goyal, A.A. Balandin, Graphene-on-Diamond devices with increased current-carrying capacity: carbon sp2-on-sp3 technology, Nano Lett. 12 (2012) 1603–1608, https://doi.org/10.1021/nl204545q.

[62] M. Asad, S. Majdi, A. Vorobiev, K. Jeppson, J. Isberg, J. Stake, Graphene FET on diamond for high-frequency electronics, IEEE Electron. Device Lett. 43 (2022) 300–303, https://doi.org/10.1109/LED.2021.3139139.

[63] S. Majdi, V. Djurberg, M. Asad, A. Aitkulova, N. Suntornwipat, J. Stake, J. Isberg, Enhanced Hall mobility in graphene-on-electronic-grade diamond, Appl. Phys. Lett. 123 (2023) 012102, https://doi.org/10.1063/5.0156108.